

Spectropolarimeter for Satellite Identification

Louis Lischwe¹, Dr. T.P.G. Wijnen², and Dr. ir. M. Rodenhuis³

¹*Faculty of Aerospace Engineering, Delft University of Technology, Delft, The Netherlands*

²*Faculty of Aerospace Engineering, Delft University of Technology, Delft, The Netherlands*

³*Leiden Observatory, Leiden University, Leiden, The Netherlands*

30.08.2022

ABSTRACT

The exponentially increasing number of Earth-orbiting satellites, as well as the pronounced importance for space military operations, impose new challenges on a functional Space Domain Awareness (SDA). A key factor for an effective SDA is the successful identification of an Earth-orbiting satellite, or object in general. Current methods are usually limited to either time-resolved photometry, spectrometry, or polarimetry. In this paper, we present the Spectropolarimeter for Satellite Identification (SSI), whose design combines these detection methods with the aim to provide a unique ‘fingerprint’ of the satellite, thereby expanding the range of satellite identification methods.

The SSI combines a dual-channel spectrometer with off-the-shelf polarization optics. Using a combination of an achromatic quarter-wave retarder, a highly chromatic multiple order retarder, a polarizing beam splitter, and two linear polarizers, all operating in the visible spectrum, a sinusoidal modulation of the linear polarization information is imprinted onto the measured spectrum. The amplitude of the signal scales with the degree of linear polarization and the phase with the angle of linear polarization. Furthermore, by using a dual channel setup, the intensity spectrum is obtained for the full spectrograph resolution. Since the full linear spectropolarimetric information is obtained in a single measurement, differential effects and drifts are strongly reduced, which simplifies the calibration. The spectrally resolved linear polarization information provides a unique approach for satellite identification, combining material and geometric response.

We plan to take measurements with the SSI using the 800 mm Ritchey-Chrétien AZ800 telescope from the Netherlands Organisation for Applied Scientific Research (TNO) at The Hague Waalsdorp. We will attempt to identify a satellite by correlating the retrieved spectropolarimetric data from different observations of the same satellite, while also reliably discriminating it from measurements of other satellites. We expect the phase angle to have a major influence on the measured spectropolarimetric data and therefore on the ability to identify the satellite.

The proof of concept to use linear channelled spectropolarimetry for satellite identification with the SSI will open up the way for further technical refinement of the instrument, an extension to low Earth orbit satellites, and the possible addition of phase angle resolved spectropolarimetric measurements to further improve the concept of a satellite’s spectropolarimetric ‘fingerprint’.

Our work is part of a collaboration between Leiden Observatory and Delft University of Technology commissioned by the Royal Netherlands Air Force. Observations are kindly supported by TNO.

1. INTRODUCTION

Due to the more cost-effective access to space caused by the new private space economy, the number of artificial objects orbiting Earth is expected to increase from the order of 10^4 today to 10^6 in 2030 [7]. Simultaneously, space has become a military domain. NATO members have to expand their military space capabilities including a comprehensive Space Domain Awareness (SDA) and the capability of satellite identification [8]. Therefore, it is of high importance that industry and academia provide innovative and cost-effective sensors for future military SDA capabilities [5].

Multiple imaging methods can be used for satellite identification and characterisation, each featuring advantages and disadvantages. The performance of resolved imaging is limited by the diffraction limit of optical telescopes [22]. Resolved imaging of geostationary satellites (GEO) has been performed, but with poor resolution and the need for large aperture telescopes [15][10], making resolved imaging an unsuited method for a quick and cost-effective sensor expansion in the SDA field. Photometry in varying complexity can be used to infer satellite characteristics [4][14]. Photometry for satellite identification has also been performed with a probability of success between 70-80 % [13][12]. Satellite spectrometry is mainly used to infer the used materials and by that identify the satellite. Successful characterisation of space debris was conducted by Reddy et al. [17] using spectral observations. Especially the time-resolved spectral behaviour of satellites has been the target of extensive research [21][9][11]. In addition to photometry and spectrometry, polarimetry has mainly been used to infer geometry characteristics [3][2]. A successful identification of GEO satellites using polarimetry was conducted by Speicher [20].

Our research combines elements of unresolved satellite imaging by using spectropolarimetric measurements for satellite identification and by this expanding on the use of general time-resolved satellite spectropolarimetry conducted before [23]. This research is a combined effort of Leiden University and Delft University of Technology commissioned by the Royal Netherlands Airforce to conduct a proof of concept for a spectropolarimeter for satellite identification. The work is conducted as part of a master thesis project.

We use a method of spectral linear polarization modulation in the form of dual-channeled spectropolarimetry based on the work of Snik et al. [19]. This snapshot method has the advantage of a straightforward instrument setup due to the absence of moving parts. The dual-channel setup can provide the intensity spectrum at full spectrograph resolution of 9 nm. Path differences are corrected by an iterative transmission algorithm. The degree and angle of linear polarization can be retrieved with an average reduced resolution of a factor of 10 due to the modulation approach. To keep it simple and cost-effective, only off-the-shelf components are used for the instrument. An 800 mm optical telescope situated at the Netherlands Organisation for Applied Scientific Research (TNO) facilities in The Hague is going to be used.

We expect this research to open up a new category of satellite identification. This will provide our defence organisations with the strongly needed and cost-effective SDA sensors.

2. TARGET DESCRIPTION

For the Spectropolarimeter for Satellite Identification (SSI) proof of concept, it was decided to concentrate on the observation of GEO satellites. This facilitates a relatively simple observation setup and calibration procedure. Additionally, the retrieved polarization information of an Earth-orbiting object is strongly dependent on the illumination geometry[23][6][1]. Therefore, the relatively stable illumination geometry aids in not mixing up polarization signatures. On the other hand, the instrument will receive a relative low photon flux due to the high orbit altitude.

The targets were chosen based on their visibility from the Netherlands and relatively good apparent visual brightness for a GEO satellite ranging around 10^{-2} . For pointing and guiding the most recent Two Line Element (TLE) and an ASI1600MM Pro tracking camera is used. A list of the satellite targets is shown in the legend of Fig. 1. We expect DoLP signals of 0 - 20 % [23].

Low target elevation angles with respect to the telescope position will cause an increased atmospheric extinction and further increase the apparent visual brightness by 0.2 - 1 based on received photon flux modelling. Additionally, observing from an urban area like The Hague increases stray light and background radiation.

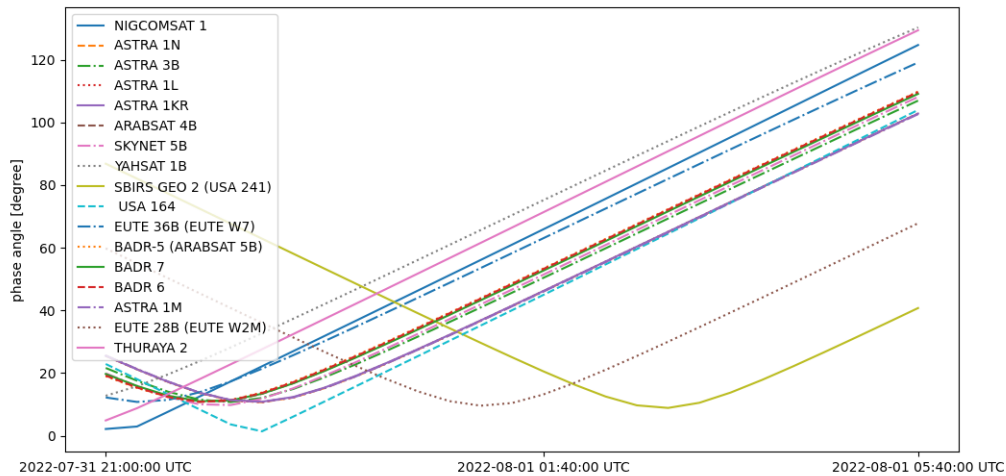


Fig. 1: Phase angle progression of target satellites for the night of 31.07.2022.

Fig. 1 depicts the phase angle progression of each target satellite for an exemplary observation night. The phase angle will depend on the season of observation, the precise orbit of the target, and the latitude and longitude of the observation location [20][16]. The intensity spectrum of the satellites will change throughout the progression of the phase angle, with an accelerated change close to a phase angle of 0° degrees, also corresponding to the highest received photon flux. This spike in reflected light, or glint, is often dominated by the satellite’s solar panels and also strongly influences the polarization signal [21]. Most of the targets are best observed at the beginning of the night, whereas the two south-west located satellites are best observed around midnight to maximize the received photon flux.

3. INSTRUMENT DESCRIPTION

Fig. 2 shows a schematic of the instrument optics mounted on the telescope. Table 1 depicts the corresponding part information. The overall instrumentation can be grouped into pre-instrument optics and the Spectropolarimeter for Satellite Identification itself. The former comprises the telescope, a non-polarizing beamsplitter, and the tracking camera. The setup was chosen to simplify alignment between the optical origin of the tracking camera and the entry slit of the spectrograph, ensuring precise pointing and tracking of the chosen GEO satellite.

The focus f_1 of the telescope can be adjusted by moving the secondary mirror.

The fast axis of the quarter-wave plate is aligned with the p-polarization axis and therefore with the transmitting direction of the polarizing beamsplitter and the followed linear polarizer. The quarter-wave plate rotates the plane spanned by the Q/I, U/I Stokes vector components to the Q/I, V/I plane. The multiple-order retarder has its fast axis offset 45° degrees from the fast axis of the quarter-wave plate. It rotates the points in the Q/I, V/I plane around the U/I axis depending on the wavelength due to its chromatic nature. The polarizing beamsplitter finally projects all points onto the Q/I axis [19].

The angular field of view of the spectrograph slit is estimated to be $0.18^\circ \times 0.14^\circ$ degrees.

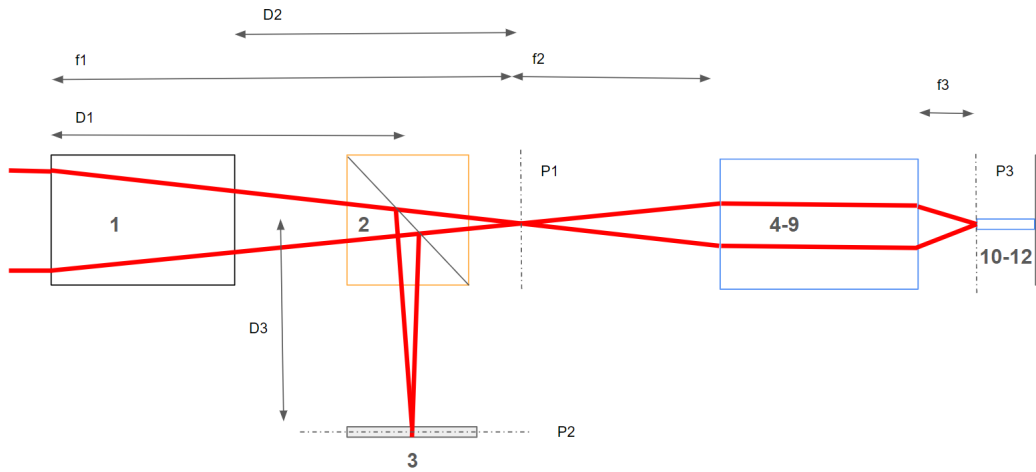


Fig. 2: Schematic of the complete optical train. Part labelling 1-12 corresponds to Table 1.
 $f_1 = 5600$ mm, $f_2 = 30$ mm, $f_3 = 34.74$ mm, $D_1 = 5442$ mm, $D_2 = 258$ mm, $D_3 = 158$ mm
 P1/P2 = telescope focal plane, P3 = fiber collimating lens focal plane

Table 1: Sequence of optical parts used for observations with the SSI.
 The part number corresponds to the labelling in Fig. 2.

Part Name	Part Number	Part Information
Ritchey-Chrétien ASA AZ800 Telescope	1	aperture = 800 mm, focal length = 5600 mm pointing accuracy ≤ 2 arcsec Nasmyth focus
Non-Polarizing Beamsplitter	2	anti-reflection coating range = 400 - 700 nm reflection-transmission ratio = 10:90
ASI1600MM Pro Tracking Camera	3	sensor with 4656×3520 pixels, pixel size = $3.8 \mu\text{m}$ angular field of view = $0.18^\circ \times 0.14^\circ$ degrees
Achromatic Lens	4	anti-reflection coating range = 400 - 700 nm focal length = 30 mm
Achromatic Quarter-Wave Retarder	5	anti-reflection coating range = 400 - 800 nm
Multiple-Order Retarder	6	dual anti-reflection coating at 532 nm and 1064 nm quarter-wave plate at 532 nm half-wave plate at 1064 nm plate thickness = 0.3038145 mm material = crystalline quartz
Polarizing Beamsplitter	7	anti-reflection coating range = 400 - 700 nm
2 x Linear Polarizer	8	anti-reflection coating range = 420 - 700 nm
2 x Fiber Collimating Lens	9	anti-reflection coating range = 350 - 700 nm focal length = 34.74 mm
Multi-Mode Fiber	10	diameter = $200 \mu\text{m}$, NA = 0.22
AVASPEC-1650F-2-USB2 Spectrograph	11	blaze wavelength = 500 nm grating = 300 l/mm for 450-900 nm slit size = $200 \times 1000 \mu\text{m}$ resolution = 9 nm
Starline Sony2048 CCD Detector	12	1650 usable pixel, pixel size = $14 \times 56 \mu\text{m}$

4. METHOD AND RETRIEVAL ALGORITHM

4.1 Linear Polarization Modulation

The Spectropolarimeter for Satellite Identification design is based on a method of spectral linear polarization modulation in the form of dual channelled spectropolarimetry [19].

The combined Mueller matrix of the optical instrument train is given by equation 1. The value of k is 1 for the p-polarized channel and -1 for the s-polarized channel.

$$\frac{1}{2} \begin{pmatrix} 1 & k \cos\left(\frac{2\pi\delta}{\lambda}\right) & -k \sin\left(\frac{2\pi\delta}{\lambda}\right) & 0 \\ k & \cos\left(\frac{2\pi\delta}{\lambda}\right) & -\sin\left(\frac{2\pi\delta}{\lambda}\right) & 0 \\ 0 & 0 & 0 & 0 \\ 0 & 0 & 0 & 0 \end{pmatrix}, \quad k = +1, -1, \quad (1)$$

Combining the instrument Mueller matrix with the Stokes vector of the incoming unmodulated beam results in the modulated Stokes vector shown by equation 2.

$$\begin{pmatrix} I(\lambda) \\ Q(\lambda) \\ U(\lambda) \\ V(\lambda) \end{pmatrix} = \frac{1}{2} \begin{pmatrix} I_0(\lambda) + Q_0(\lambda) k \cos\left(\frac{2\pi\delta}{\lambda}\right) - U_0(\lambda) k \sin\left(\frac{2\pi\delta}{\lambda}\right) \\ I_0(\lambda) k + Q_0(\lambda) \cos\left(\frac{2\pi\delta}{\lambda}\right) - U_0(\lambda) \sin\left(\frac{2\pi\delta}{\lambda}\right) \\ 0 \\ 0 \end{pmatrix} \quad (2)$$

The measured modulated signals of the s- and p-polarized channel by the spectrometer are then given by equation 3 and 4 respectively, where q and u are the normalized Stokes vector components [18].

$$I_p(\lambda) = \frac{1}{2} I_0(\lambda) \left\{ 1 + q(\lambda) \cos\left(\frac{2\pi\delta}{\lambda}\right) - u(\lambda) \sin\left(\frac{2\pi\delta}{\lambda}\right) \right\} \quad (3)$$

$$I_s(\lambda) = \frac{1}{2} I_0(\lambda) \left\{ 1 - q(\lambda) \cos\left(\frac{2\pi\delta}{\lambda}\right) + u(\lambda) \sin\left(\frac{2\pi\delta}{\lambda}\right) \right\} \quad (4)$$

Using mathematical manipulations and the definitions for the degree of linear polarization (DoLP) and angle of linear polarization (AoLP) given by equations 5a and 5b respectively results in the final modulation equations given by equation 6 denoting the differential transmission of both channels by $t(\lambda)_{p/s}$.

$$P_L = \frac{\sqrt{Q^2 + U^2}}{I} \quad (5a)$$

$$\phi = \frac{1}{2} \tan^{-1} \left(\frac{U}{Q} \right) \quad (5b)$$

$$I_{p/s}(\lambda) = \frac{1}{2} I_0(\lambda) t(\lambda)_{p/s} \left\{ 1 \pm P_L(\lambda) \cos\left(\frac{2\pi\delta(\lambda)}{\lambda} + 2\phi(\lambda)\right) \right\} \quad (6)$$

An example of the modulation principle is given in Fig. 3. The relative modulation signal for both channels after the division of equation 6 by I_0 is shown. The high amplitude modulation is simulated with a DoLP = 1 and AoLP = 0° degrees. The lower amplitude modulation is simulated with a DoLP = 0.5 and AoLP = 45° degrees. The modelling was conducted with the characteristics of the multiple-order retarder used in the actual SSI setup. For the shown wavelength range of 400 - 800 nm, this corresponds to an average local modulation period of 135 nm. The decrease in amplitude and shift in phase are clearly visible.

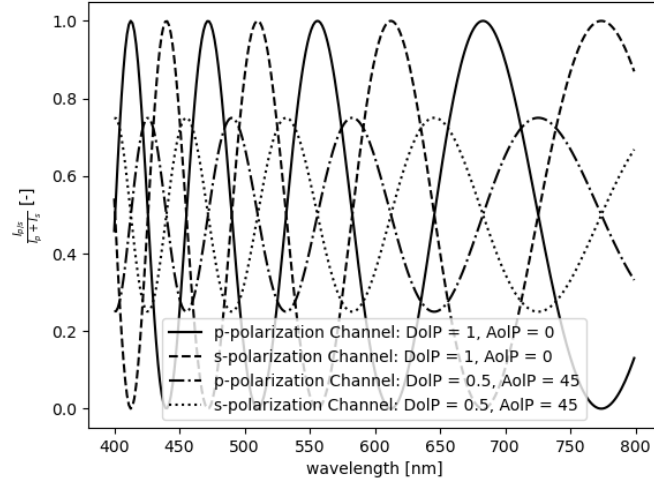


Fig. 3: Relative modulation signal for DoIP = 1/AoIP = 0° degrees and DoIP = 0.5/AoIP = 45° degrees.

4.2 Retrieval Algorithm

Fig. 4 gives an overview of the retrieval algorithm to extract the linear polarization information modulated onto the measured satellite spectrum. The algorithm can be divided into operations for iterative transmission correction (red), calibration measures (blue), and fitting operations (black). This section concentrates on transmission correction and fitting operations. The calibration measures and results are shown in section 5.

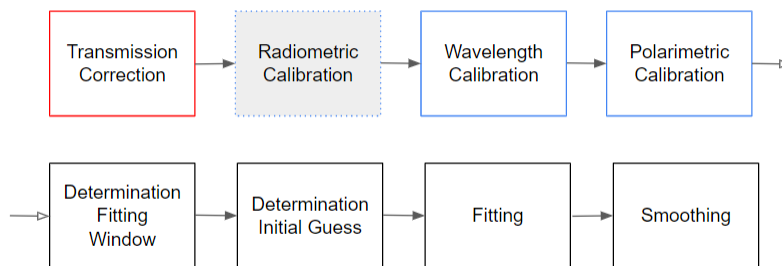


Fig. 4: Calibration and retrieval algorithm for the polarization information.

Transmission Correction

An exact determination of the differential transmission of both channels is hard to determine due to the off-the-shelf nature of the instrument. In addition, transmission per channel is prone to change with time. Therefore, an iterative transmission correction is applied.

The normalized difference between both channels is given by equation 7, where $t(\lambda)$ is defined as $\frac{t(\lambda)_s}{t(\lambda)_p}$. The equation is used to perform a fit to the measured normalized difference over one modulation period. The difference to the measured normalized difference can be attributed to the higher frequency components of the transmission difference and can be corrected for. Iteratively varying the upper bound for $P_L(\lambda)$ based on the variance of ϕ prevents a false modulation of $P_L(\lambda)$ for a non-smooth transmission difference and allows the algorithm to converge to the true $t(\lambda)$.

$$\frac{\frac{1}{2} \left\{ 1 + P_L(\lambda) \cos \left(\frac{2\pi\delta(\lambda)}{\lambda} + 2\phi(\lambda) \right) \right\} - \frac{1}{2} t(\lambda) \left\{ 1 - P_L(\lambda) \cos \left(\frac{2\pi\delta(\lambda)}{\lambda} + 2\phi(\lambda) \right) \right\}}{\frac{1}{2} \left\{ 1 + P_L(\lambda) \cos \left(\frac{2\pi\delta(\lambda)}{\lambda} + 2\phi(\lambda) \right) \right\} + \frac{1}{2} t(\lambda) \left\{ 1 - P_L(\lambda) \cos \left(\frac{2\pi\delta(\lambda)}{\lambda} + 2\phi(\lambda) \right) \right\}} \quad (7)$$

Fitting Operations

The general idea of the retrieval algorithm is to create a spectral window for which the polarization information is estimated by fitting equation 3 or 4 to the measured intensity data points. For the best fit, the fitting window should cover one period of the cosine modulation, which on the other hand reduces the resolution of the retrieved polarization data accordingly.

For each wavelength point measured by the spectrograph, a spectral window is created with the data point as the centre. As the modulation is not periodic in λ , but in $\frac{1}{\lambda}$, and the retardance $\delta(\lambda, T)$ is itself a function of wavelength, there is not going to be a fixed period when analysing the modulated spectrum. The local modulation period can be approximated by $\frac{\lambda^2}{\delta}$ for $\delta \gg \lambda$. Therefore, the width of the spectral window is quadratic in wavelength and will grow with the local modulation period as the wavelength shifts to the red. Some spectral windows located at the edges of the measured spectrum will therefore not have full coverage of data points and are omitted.

In a second step, the intensity spectrum $I_0(\lambda)$ for each measured data point is calculated by summing the modulated spectrum for each channel.

The measured spectrum is then divided by the intensity spectrum $I_0(\lambda)$ to normalize the data.

A first estimate of P_L for each spectral window is derived by looking at the minimum and maximum data of the normalized measured intensity.

The initial estimate of ϕ is derived by fitting $\cos^2(\lambda + \lambda_\phi)$ to a cross-correlation of the measured normalized signal and a created normalized reference signal with $P_L = 1$, and $\phi = 0$.

Using the initial estimates for each spectral window and applying the boundaries $0 \leq \phi \leq \pi$ and $0 \leq P_L \leq 1$ the final fit of equation 3 or 4 in the normalized form to the normalized measured spectrum is conducted. The value for $\delta(\lambda)$ is taken from literature [19].

5. LABORATORY TESTING

This section covers the calibration measures shown in Fig. 4 as well as laboratory validation measurements.

5.1 Calibration

The modulation equations 3 and 4 represent the theoretical relations without errors. Those errors can be summarized in an efficiency term $W(\lambda)$ as shown in equation 8 [18]. The polarimetric efficiency is mainly dominated by the slit function or instrument response function, more prominent in the short wavelength region due to the higher modulation frequency. Other main contributing errors amongst others are misalignment, retardance offset and temperature effects[19].

$$\begin{aligned} \langle I_p \rangle(\lambda) &= \frac{1}{2} I_0(\lambda) \left\{ 1 + W(\lambda) \left(q \cos \left(\frac{2\pi\delta}{\lambda} \right) - u \sin \left(\frac{2\pi\delta}{\lambda} \right) \right) \right\} \\ \langle I_s \rangle(\lambda) &= \frac{1}{2} I_0(\lambda) \left\{ 1 - W(\lambda) \left(q \cos \left(\frac{2\pi\delta}{\lambda} \right) - u \sin \left(\frac{2\pi\delta}{\lambda} \right) \right) \right\} \end{aligned} \quad (8)$$

Laboratory calibration was done using a laser driven light source in combination with an integrating sphere to ensure a non-polarized input signal. Wavelength calibration was conducted using a Mercury-Argon spectral line lamp. After the laboratory calibration campaign, we performed validation measurements using a double glass plate setup to induce low levels of DoIP.

Wavelength Calibration

To infer a possible wavelength drift of the used dual channel spectrograph we fitted a Gaussian distribution to the detected peaks and compared the estimated mean to the reference values for each spectra line.

The absolute difference for both channels to the indicated spectral lines is given by Fig. 5. The maximum drift is smaller than 2.8 nm and therefore around one-third of the spectral resolution. Nevertheless, we updated the coefficients of the polynomial to convert pixel values to a unit of wavelength by fitting a fourth-order polynomial through the usable spectral lines for both channels separately.

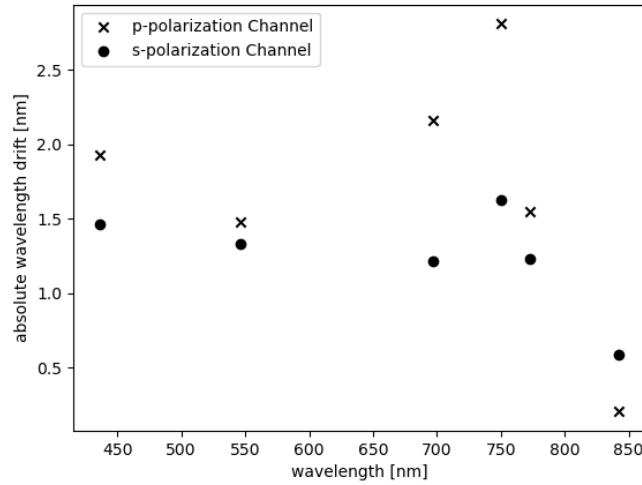


Fig. 5: Absolute wavelength drift of used dual channel spectrograph with respect to reference Mercury-Argon spectral line lamp.

Polarimetric Calibration

In a first step, a measurement of the unpolarized input signal is taken to analyse if the instrument itself induces a polarization signal which has to be corrected for. Fig. 6 shows the normalized difference between the p and s-polarization channel given by equation 7. After transmission correction, a possible polarized signal would be a cosine centred around 0 with an amplitude equal to the DoLP. Therefore, Fig. 6 indicates that there is no measurable induced polarization by the instrument itself.

For the determination of the polarimetric efficiency, a linear polarizer is used to 100% polarize the input signal. A generalized form of the normalized measured count given by equation 8 is depicted by equation 9 for the s-polarized channel, where β is the input AoLP. This indicates, that the measured output for an input signal modified by a linear polarizer turned over 360° degrees undergoes a double period variation. An example is depicted in Fig. 7 for a wavelength of 500 nm. Equation 10 is therefore fitted to the measured signal for each wavelength point in order to estimate the coefficients M_1 , M_2 , and M_3 . Equations 11 and 12 are then used to calculate the polarimetric efficiency. The procedure is repeated for the p-polarized channel.

$$\frac{I_s(\lambda)}{I_0(\lambda)} = \frac{1}{2}t(\lambda)_s \{1 + \cos 2\beta m_{S,q} + \sin 2\beta m_{S,u}\} \quad (9)$$

$$f_{\text{fit}}(\beta) = M_1 + \cos 2\beta M_2 + \sin 2\beta M_3 \quad (10)$$

$$m_{S,q} = \frac{M_2}{M_1}; \quad m_{S,u} = \frac{M_3}{M_1} \quad (11)$$

$$W_S(\lambda) = \sqrt{(m_{S,q}(\lambda))^2 + (m_{S,u}(\lambda))^2} \quad (12)$$

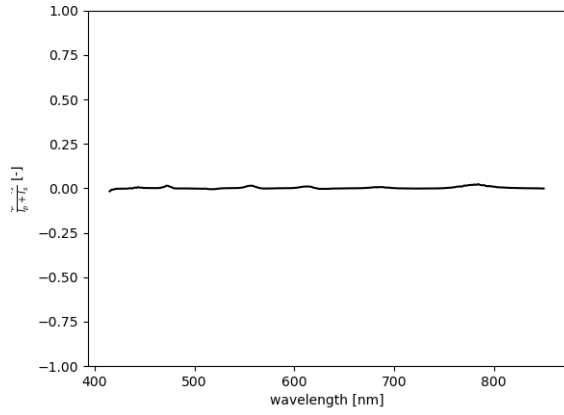


Fig. 6: Normalized difference between p and s-polarization channel for unpolarized input signal.

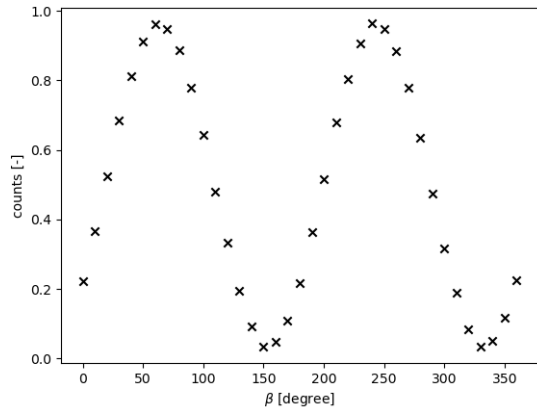


Fig. 7: Double period variation for a wavelength of 500 nm and a varying input angle of linear polarization β .

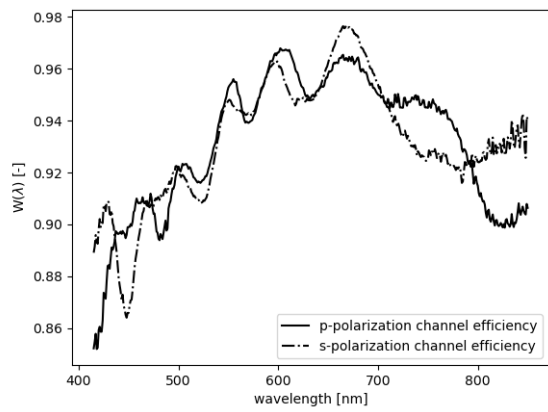


Fig. 8: Polarimetric efficiency for p- and s-polarization channel.

The resulting efficiency for the p- and s-polarization channel is shown in Fig. 8.

The polarimetric efficiency is not equal for both channels. The modulation pattern is probably caused by a misalignment of the components introducing small sinusoidal terms as can be expected for an off-the-shelf setup. The relative lower efficiency for the blue side of the spectrum reflects the influence of the slit function. The reduced efficiency at the red end of the spectrum could be caused by the range of the anti-reflection coatings of the optical components.

5.2 Validation

The induced polarization by the double glass plate setup was calculated by using the Fresnel equations and the wavelength-dependent refractive indices for the used BK7 glass. The retrieved and theoretical values of DoIP for a glass plate angle ranging from 20° - 60° degrees is shown in Fig. 9a. The absolute error between calculated and retrieved values is depicted in Fig. 9b. The SSI seems to be able to reproduce the theoretical values with an accuracy $\leq 1.2\%$ DoIP, more accurate for higher values of induced DoIP. The validation of sensitivity was limited by the angle resolution of the glass plate setup. Nevertheless, it was shown that the SSI is able to distinguish DoIP signals $\geq 1.3\%$ in a laboratory environment.

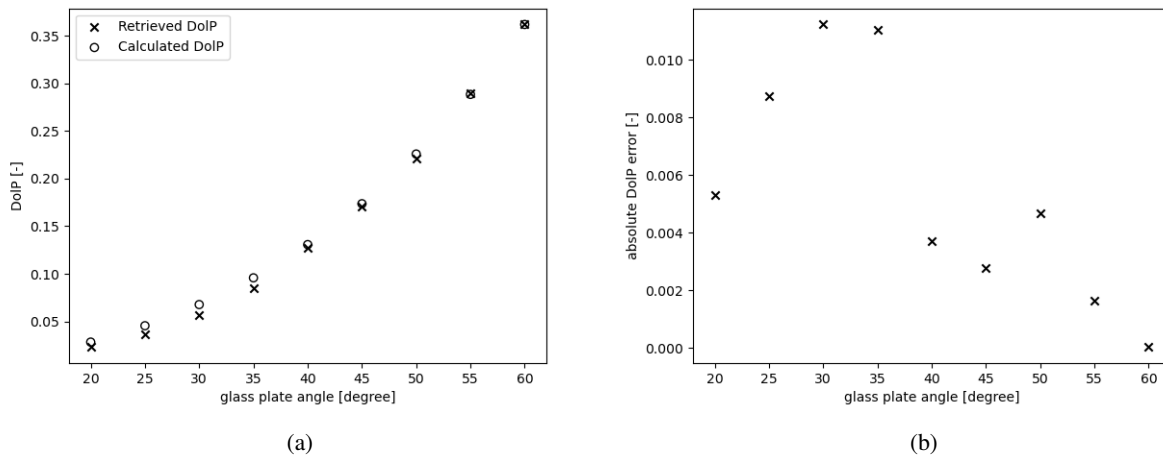


Fig. 9: a) Calculated DoIP by the glass plate setup and retrieved DoIP.
b) Absolute Difference between calculated and retrieved DoIP.

6. PRELIMINARY OBSERVATIONS

Due to complications with the instrument alignment process on the telescope and time constraints we were only able to take example observations of stars until now. The measurements suffer from a reduced signal-to-noise ratio due to a discrepancy in received photons.

On the night of 14.07.2022, we took observations of HD 124897 ('Arcturus') and HD 8890 ('Polaris')¹. Dark noise correction and pixel averaging were performed on both measurements. The measured spectrum and retrieved DoIP for Arcturus is depicted in Fig. 10a and Fig. 10b. The respective measurements for Polaris are shown in Fig. 11a and Fig. 11b. Fig. 10b shows a retrieved DoIP between 0 and 5%. As the linear polarization level of Arcturus is too low to be detected by the SSI, the retrieved DoIP might reflect the induced polarization by the M3 mirror of the telescope Nasmyth port and the non-polarizing beamsplitter. The induced polarization has not been modelled yet, but the level reflects expected values from literature, although more steady values over the wavelength range are more reasonable. The retrieved DoIP for Polaris is basically zero and probably an artefact of the iterative transmission correction. We expect that the observed signals are compromised by the low signal-to-noise ratio partly or over the whole wavelength range. Therefore, the SSI is not able to retrieve the correct induced polarization signal.

¹HD = Henry Draper Star Catalogue

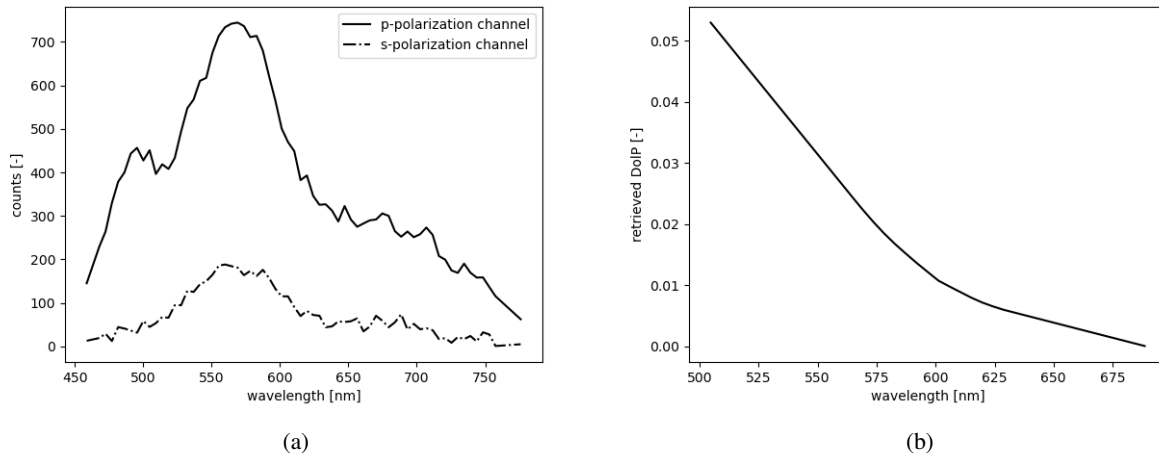


Fig. 10: a) Measured spectrum of HD 124897 ('Arcturus') on the night of 14.07.2022.
b) Retrieved DoIP of HD 124897.

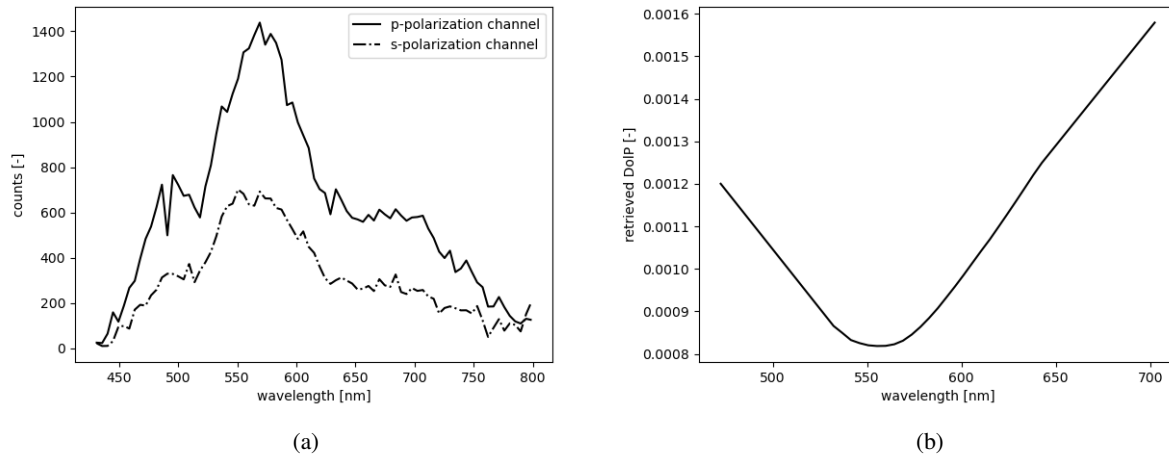


Fig. 11: a) Measured spectrum of HD 8890 ('Polaris') on the night of 14.07.2022.
b) Retrieved DoIP of HD 8890.

7. CONCLUSION AND FUTURE WORK

We built the Spectropolarimeter for Satellite Identification based on a method of spectral linear polarization modulation in the form of dual channelled spectropolarimetry which enables us to retrieve the linear polarization information of a target in a snapshot manner. The instrument is straightforward to set up using off-the-shelf optics. We performed laboratory wavelength and polarimetric calibration of the instrument. Laboratory validation using a double glass plate setup indicates an accuracy of $\leq 1.2\%$ DoIP. In the laboratory, we are able to distinguish DoIP signals $\geq 1.3\%$. Due to alignment issues and a discrepancy in received photons, we have not been able to observe the target satellites yet. Retrieved signals of star observations indicate DoIP levels of induced instrumental polarization. It is expected that the measurements are compromised by low signal-to-noise ratios.

Our next steps are focused on investigating the discrepancy in received photons, boosting the signal-to-noise ratio, and taking spectropolarimetric measurements of the chosen GEO target satellites. Subsequently, we will try to perform the satellite identification and work on an extension to lower Earth-orbiting satellites.

8. REFERENCES

- [1] Adam Battle, Vishnu Reddy, Roberto Furfaro, Tanner Campbell, James Frith, and David Monet. A visible spectral atlas of geostationary satellites. 2021.
- [2] D. K. Beamer. *Polarization Signatures in Vector Space*. PhD thesis, University of Dayton, 2018.
- [3] D. K. Beamer, U. Abeywickrema, and P. Banerjee. Polarization vector signatures for target identification. In *Polarization Science and Remote Sensing VIII*, volume 10407, pages 208–214. SPIE, 2017.
- [4] Shane Bruski, Samuel R. Harms, Micheal P. Jones, Neil Thomas, and Scott R. Dahlke. Determination of satellite characteristics through visible light intensity analysis. In *AMOS 2012 Conference Proceedings*, page 9, 2012.
- [5] DeAnna Maria Burt. AMOS 2021 conference opening presentation. In *AMOS 2021 Conference Proceedings*, 2021.
- [6] Major Donald Bédard, Gregg A Wade, and Dmitry Monin. Spectrometric characterization of geostationary satellites. In *AMOS 2012 Conference Proceedings*, 2012.
- [7] Eric Col Felt and Joseph Col Roth. The space s&t challenges fom LEO to cislunar. In *AMOS 2021 Conference Proceedings*, 2021.
- [8] United States Space Command. Commander’s strategic vision. <https://www.spacecom.mil/Mission/Commanders-Strategic-Vision/>. Accessed: 2021-12-17.
- [9] Augustine J DeMeulenaere, Eli Q Harmon, and Francis K Chun. Simultaneous glint spectral signatures of geosynchronous satellites from multiple telescopes. In *AMOS 2018 Conference Proceedings*, 2018.
- [10] Jack D Drummond and Richard H Rast. First resolved images of a spacecraft in geostationary orbit with the keck-II 10 m telescope. In *AMOS 2010 Conference Proceedings*, 2010.
- [11] Anita N. Dunsmore, Joshua A. Key, Ryan M. Tucker, Evan M. Weld, Francis K. Chun, and Roger D. Tippets. Spectral measurements of geosynchronous satellites during glint season. *Journal of Spacecraft and Rockets*, 54(2):349–355, 2017.
- [12] Daniel O. Fulcoly, Katharine I. Kalamaroff, and Francis K. Chun. Determining basic satellite shape from photometric light curves. *Journal of Spacecraft and Rockets*, 49(1):76–82, 2012.
- [13] Roberto Furfaro, Richard Linares, and Vishnu Reddy. Space objects classification via light-curve measurements: Deep convolutional neural networks and model-based transfer learning. In *AMOS 2018 Conference Proceedings*, 2018.
- [14] Yi Han, Huayan Sun, Jianguang Feng, and Liang Li. Analysis of the optical scattering characteristics of different types of space targets. *Measurement Science and Technology*, 25(7), 2014.
- [15] Michael Hart, Richard Rast, Stuart Jefferies, and Douglas Hope. Resolved observations of geostationary satellites from the 6.5 m MMT. In *AMOS 2015 Conference Proceedings*, 2015.
- [16] Jeremy Murray-Krezan, Willa C Inbody, Phan Dao, Anthony Dentamaro, Daniel Fulcoly, and Stephen A Gregory. Algorithms for automated characterization of three-axis stabilized GEOs using non- resolved optical observations. In *AMOS 2012 Conference Proceedings*, 2012.
- [17] Vishnu Reddy. Spectral characterization of 2020 SO. In *AMOS 2021 Conference Proceedings*, 2021.
- [18] Martijn Smit, Jeroen Rietjens, Jochen Campo, Joost aan de Brugh, Aaldert van Amerongen, Otto Hasekamp, Jochen Landgraf, and Xin Liu. Polarimetric calibration of a spectro-polarimeter for remote sensing and characterization of aerosols. In *International Conference on Space Optics — ICSO 2020*, page 108. SPIE, 2021-06-11.
- [19] Frans Snik, Theodora Karalidi, and Christoph U. Keller. Spectral modulation for full linear polarimetry. *Applied Optics*, 48(7):1337–1346, 2009. Number: 7.
- [20] Andy Speicher. Identification of geostationary satellites using polarization data from unresolved images. *Electronic Theses and Dissertations*, 2015.
- [21] Daniel E Weisz, Anita N Dunsmore, Joshua A Key, Ryan M Tucker, Evan M Weld, Francis K Chun, and Roger D Tippets. Comparison of geosynchronous satellites spectral signatures during glint season. In *AMOS 2016 Conference Proceedings*, 2016.
- [22] James Richard Wertz, David F. Everett, and Jeffery John Puschell. *Space Mission Engineering: The New SMAD*. Microcosm Press, 2011.
- [23] L A Zimmerman, S S Chun, M F Pirozzoli, M K Plummer, and F K Chun. Near-simultaneous polarization and spectral optical measurements of geosynchronous satellites. In *AMOS 2020 Conference Proceedings*, 2020.